

Coseismic deformation and slip distribution of the 1997 M_w 7.5 Manyi, Tibet, earthquake from InSAR measurements

Hua Wang^{a,*}, Caijun Xu^a, Linlin Ge^b

^a School of Geodesy and Geomatics, Wuhan University, 129 Luoyu Road, Wuhan 430079, China

^b School of Surveying Spatial Information Systems, The University of New South Wales, Sydney, NSW 2052, Australia

Received 28 September 2006; received in revised form 12 March 2007; accepted 13 March 2007

Abstract

We use interferometric synthetic aperture radar (InSAR) observations to investigate the coseismic deformation and slip distribution of the 1997 M_w 7.5 Manyi earthquake, a left-lateral strike-slip earthquake occurred on the west portion of the Kunlun fault in the northern Tibet, China. The fault trace is constrained by the combination of interferometric coherence image and azimuth offset image. The total length of the identified fault is about 170 km. We estimate the source parameters using a seven-segment fault model in a homogeneous elastic half-space. We first use a uniform slip model to estimate the slip, width, dip and rake for each segment, resulting in a maximum slip of 5.5 m with a depth of 11 km on the fourth segment. The average dip of the uniform slip model is about 93° northward and the average rake is about -2° . We then use a distributed slip model to estimate the pure strike-slip and oblique slip distribution, respectively. In the distributed slip model, the fault plane is discretized into 225 patches, each of them $4 \text{ km} \times 4 \text{ km}$. We fix the optimal geometric parameters and solve for the slip distribution using a bounded variable least-squares (BVLS) method. We find a geodetic moment of $1.91 \times 10^{20} \text{ Nm}$ (M_w 7.5), of which almost 68% released in the uppermost 8 km and 82% in the uppermost 12 km. For all the models used in this study, the synthetic profiles along strike show asymmetric displacements on the opposite sides of the fault, which are in agreement with the observations. This suggests that a linear elastic model with variable and non-vertical dips is also reasonable for the mechanism of the Manyi earthquake.

© 2007 Elsevier Ltd. All rights reserved.

Keywords: Manyi earthquake; InSAR; Uniform slip; Distributed slip; Linear elastic; Asymmetry

1. Introduction

The Kunlun fault is one of the largest strike-slip faults in the Tibetan plateau. It locates at the south of the Altyn Tagh fault and extends almost 1200 km from the northeast Tibet, separating the Qaidam Basin to the northeast from the plateau (Fig. 1). Using satellite imagery, [Tapponnier and Molnar \(1977\)](#) found a number of secondary strike-slip faults, including the Manyi fault, at the west end of the Kunlun fault. The latest earthquake associated with these faults is the 4 July 1973 M_s 7.4 event, which might reactivate these secondary faults ([Tapponnier and Molnar, 1977](#)). Global Positioning System (GPS) observations and geological investigations show a left-lateral strike-slip rate of 10–14 mm/year on the Kunlun fault (e.g., [Wang et al., 2001](#); [Zhang et al., 2004](#); [Van der Woerd et al., 2000](#)).

* Corresponding author. Fax: +86 27 68778890.

E-mail address: ehwang@163.com (H. Wang).

¹ Present address: Guangdong University of Technology, China.

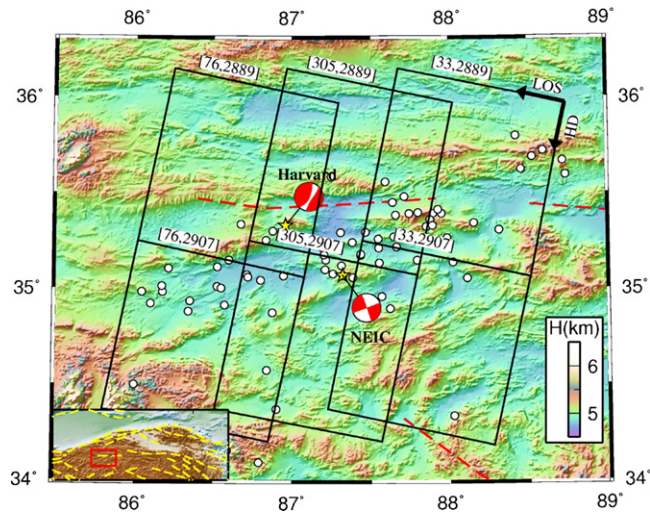


Fig. 1. Shaded relief map of the epicentral area of the 1997 Manyi earthquake. Data shown are 3 arc-second data from the SRTM. Latitude and longitude values are shown on the coordinates. The squares delimited by full lines denote radar scenes from descending orbits (track 76/305/33, frames 2889 and 2907). Two black arrows indicate the satellite look direction (ground to satellite, LOS) and its flight direction (HD). Focal mechanisms from Harvard and NEIC are shown. The small open circles denote the aftershocks.

On 8 November 1997, a M_w 7.5 earthquake occurred on the Manyi fault with its epicenter at (35.069°N, 87.325°E) (from USGS). Velasco et al. (2000) estimated the broadband source process using four distinct methods, including a master event technique, surface and body wave inversion techniques, and an empirical Green's function technique. Their estimated moment is 2×10^{20} Nm (M_w 7.5), most released in the uppermost 15 km within the first 20 s, and then continued westward for another 20–30 s. They obtained a focal mechanism of strike 225°, dip 76°, and rake 175°.

Because the quake occurred in a remote and uninhabited area, InSAR has played an important role in studying the Manyi earthquake. Peltzer et al. (1999) obtained an asymmetric coseismic displacement map using radar imagery acquired by the satellite ERS-2. The asymmetric pattern could not be well modeled using a linear elastic model with a straight vertical fault, therefore they suggested a nonlinear model with a ratio of 2 between compressive and tensile elastic moduli. With the same radar imagery, Funning (2005) fitted the observations almost as well as Peltzer et al. (1999), while using a linear elastic model with more complex fault geometry. Funning (2005) ascribed the asymmetry to a reversal of dip between the eastern and the western sides of the hypocenter.

In this study, we will analyze the same radar imagery as used by Peltzer et al. (1999) and Funning (2005) to derive the coseismic deformation associated with the Manyi earthquake. We will estimate the slip distribution along the fault with a complex fault geometry constrained by interferometric coherence image and azimuth offset image. Two unusual characteristics of the Manyi earthquake will also be discussed, i.e., the asymmetric deformation and the lack of aftershocks.

2. Data analysis

2.1. Coseismic deformation

We use radar imagery acquired by the European satellite ERS-2 before and after the Manyi earthquake from descending orbits. Because the surface rupture is very long, the imagery cover three adjacent tracks 76, 305, and 33 (Table 1). We process the radar imagery using two-pass method (Massonnet et al., 1993). The precise orbits distributed by the Delft Institute for Earth-Oriented Space Research (DEOS) are used in the interferometry (Scharroo and Visser, 1998). The topographic contribution to the interferometric phase is removed using the 3 arc-second digital elevation model (DEM) data from the Shuttle Radar Topography Mission (SRTM) (Farr and Kobrick, 2000). The SNAPHU software is used to unwrap the interferograms (Chen, 2001). The interferogram IP2 was split into two halves by the long rupture, so we must unwrap its upper and lower sides separately. After interferometric processing, we get three pairs of geocoded coseismic displacement maps covering three tracks.

Table 1
Interferometric pairs used in this study

No. ^a	Interferometric pair (yyymmdd)	B_{\perp} ^b (m)	T ^c (day)	Track
IP1	970316–971116	64	245	76
IP2	970819–971202	–9	105	305
IP3	970522–971218	–76	210	33
IP4	971116–980125	–388	70	76
IP5	971202–980106	–120	35	305
IP6	971218–980122	–306	35	33

All imagery are from the frames 2889 and 2907.

^a IP1–IP3 are coseismic interferometric pairs, and IP4–IP6 are postseismic pairs.

^b B_{\perp} corresponds to the perpendicular baseline.

^c T corresponds to the temporal baseline.

We mosaic the above interferograms and produce a rewrapped map in Fig. 2. During mosaicing, we project the line-of-sight (LOS) displacements from variable look directions into a uniform angle of 23° , and eliminate the constant offsets between adjacent interferograms caused by phase unwrapping and orbit errors. Thus, the fringes are more continuous than Peltzer et al. (1999) between adjacent interferograms.

2.2. Fault trace

The Manyi earthquake occurred in a remote and uninhabited area in the Tibetan plateau, so it is difficult to map the fault rupture through field surveying. Whereas, the interferometric coherence image and azimuth offset image are capable of identifying fault trace accurately (e.g., Peltzer et al., 1999; Simons et al., 2002). The lack of vegetation in the Tibetan plateau allows high correlation between radar images, which makes it excellent to identify the fault trace using coherence and azimuth offset information.

To identify the fault trace, we have to distinguish between the temporal decorrelation and the decorrelation due to large-gradient deformation. To remove the temporal decorrelation, we propose a threshold exclusive or (TXOR) algorithm to process the coseismic (IP1–IP3) and the postseismic (IP4–IP6) pairs (Fig. 3a and b). We suppose the coherence values of γ_1 and γ_2 for a pixel in the coseismic and the postseismic pairs, respectively. Given a threshold γ_0 , the resultant coherence is

$$\gamma = \begin{cases} \gamma_1, & (\gamma_1 - \gamma_0)(\gamma_2 - \gamma_0) \leq 0 \\ 1.0, & (\gamma_1 - \gamma_0)(\gamma_2 - \gamma_0) > 0 \end{cases} \quad (1)$$

The threshold of 0.3 is used in this study. Different from the decorrelation due to large-gradient deformation, the temporal decorrelation will reduce the coherence in both the coseismic and the postseismic (or preseismic) pairs.

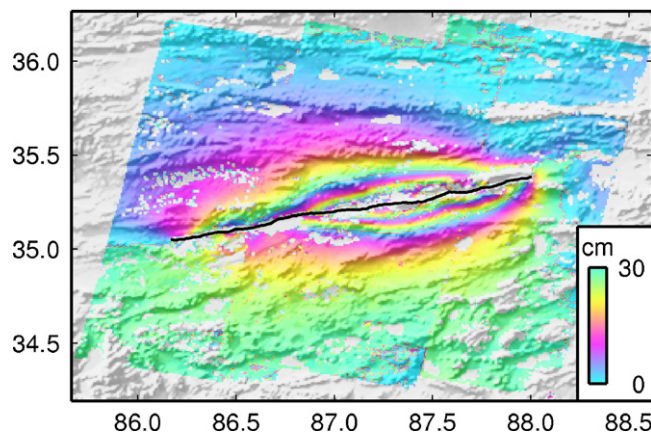


Fig. 2. Rewrapped interferogram showing the coseismic deformation due to the Manyi earthquake. Each color cycle represents 30 cm of displacement in the LOS direction.

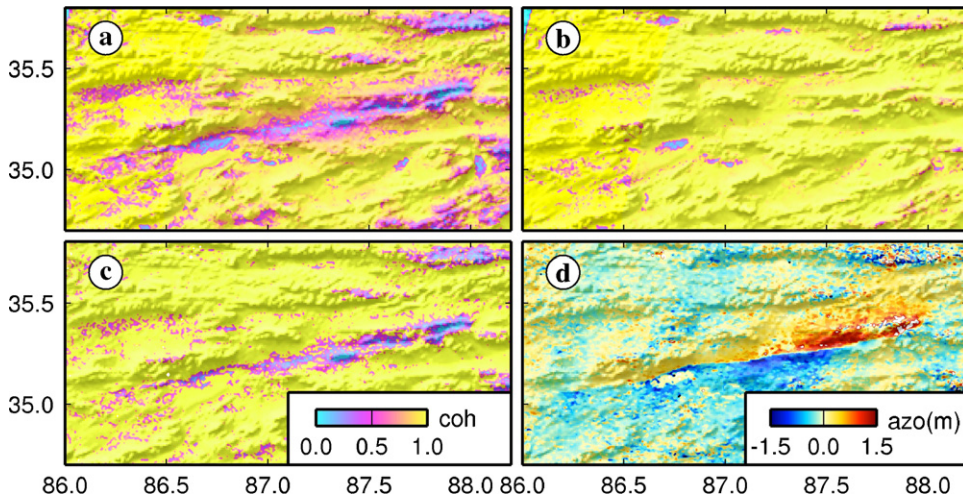


Fig. 3. Identifying fault trace using the interferometric coherence image and the azimuth offset image. (a) A mosaic of the coseismic coherence images. (b) A mosaic of the postseismic coherence images. (c) Resultant coherence image by the TXOR algorithm. (d) A mosaic of the coseismic azimuth offset images.

Therefore, it can be partly removed using our TXOR algorithm (Fig. 3c). The degree of removal depends on the difference between the coseismic and the postseismic (or preseismic) temporal baselines.

The azimuth offsets are initially estimated using intensity cross-correlation method. A quadratic trend is then removed from the estimations in order to mitigate the systematic offset due to orbit errors (Fig. 3d) (see Wang et al., 2007 for details).

We extract the fault trace from the coherence image and the azimuth offset image, respectively (Fig. 4). They are in good agreement with each other along almost the full length of the fault. At the eastern end, the azimuth offset image shows even clearer fault trace than the coherence image. This segment is striking northward relative to the western segments. The complex fault trace is approximated as seven segments for the following slip inversion (Fig. 4).

3. Modeling

3.1. Data reduction and weighting

Considering different orbit errors in different tracks, we model the source parameters using the original displacements instead of the mosaic map in Fig. 2. The three pairs of displacement maps yield $\sim 5 \times 10^7$ data points, so that it is impractical to use all the data. We first average the data over 4×4 -pixel bins, giving a minimum posting of ~ 180 m. Then we reduce the data using a quadtree algorithm (e.g., Jónsson et al., 2002). The algorithm divides the whole image into quadrants and then calculate the root-mean-square (RMS) in each quadrant. If the RMS exceeds a given threshold,

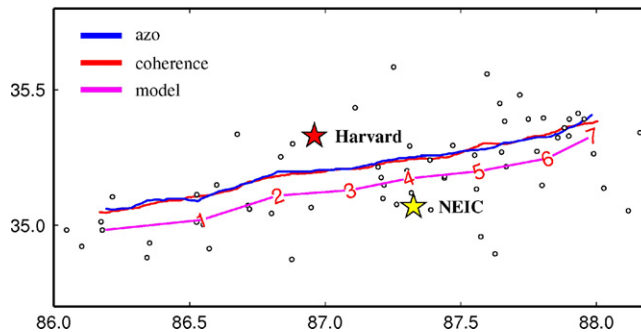


Fig. 4. Fault trace identified from Fig. 3c–d. The seven-segment fault model for slip inversion is plotted together with the segment numbers beneath the identified fault trace.

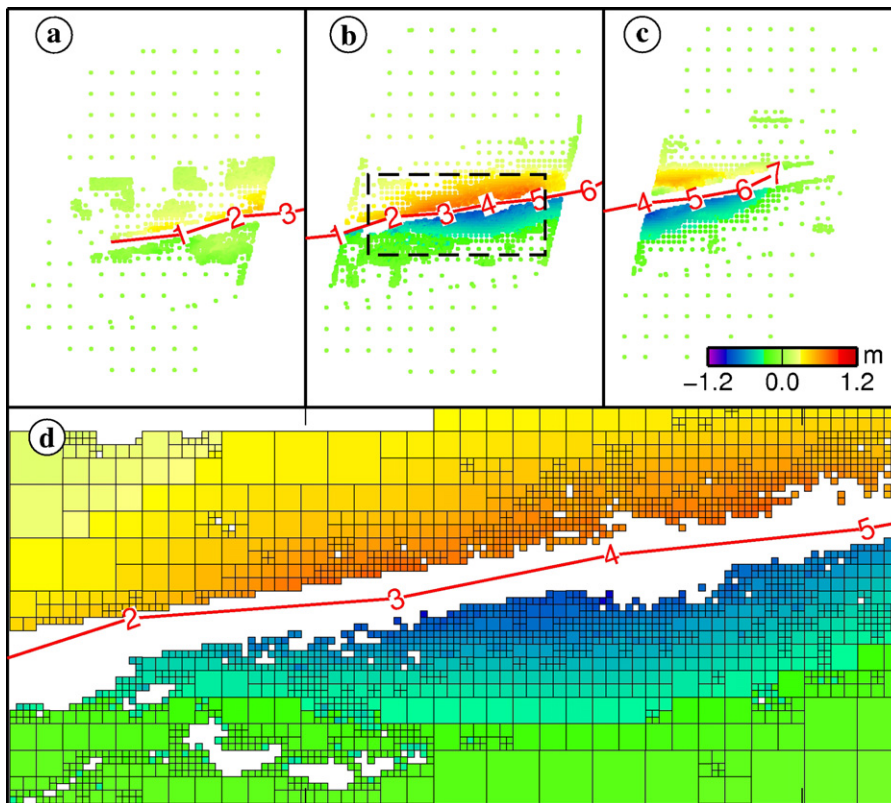


Fig. 5. (a–c) Down-sampled LOS displacements from IP1–IP3 using quadtree algorithm. The regions of Fig. 5a–c are the same with those of Fig. 6a–c, respectively. (d) Box closed fault zone in Fig. 5b.

the quadrant is further subdivided into four. Otherwise, the average value in the quadrant is the output. This process is recursively executed until the size of the quadrant equals to a given minimum. The pixels farther than 40 km away from the fault are sampled on a relatively sparse regular grid with spacing of $10 \text{ km} \times 10 \text{ km}$. The pixels closer than 2 km to the fault are eliminated in order to take into account uncertainties on the fault location (Lasserre et al., 2005). The ratio of valid pixels in a quadrant must be higher than a given level, e.g., 0.9 in this study, to deal with the irregular boundaries in the deformation maps (Masterlark and Lu, 2004). Using the above strategies, only 6576 data points are left in the down-sampled data sets (Fig. 5, Table 2).

To ensure a balanced contribution of different data sets in a joint inversion, reasonable weights should be assigned to the observations. In this study, we use the following weighting strategies. Within a particular data set, the weight ratio of individual point is proportional to the quadrant size during down-sampling. Among the data sets, a ratio is given to each data set to keep a balance of residuals. The resultant weight for each data point is expressed in Eq. (2), and the sum of weights equals unity, i.e., Eq. (3).

Table 2
Number of data points, weight ratio, RMS and moment

No.	Data points	Weight ratio (%)	σ_1 (mm) ^a	σ_2 (mm)	σ_3 (mm)	M_0^1 (10^{20} Nm) ^b	M_0^2 (10^{20} Nm) ^b	M_0^3 (10^{20} Nm)
IP1	1781	25	40	38	30			
IP2	3237	50	40	32	27	–	–	–
IP3	1558	25	49	41	37			
Total	6576	100	41	36	30	1.77	1.99	1.91

^a σ_1 , σ_2 , and σ_3 are the RMS values for Model 1, Model 2 and Model 3, respectively.

^b M_0^1 , M_0^2 , and M_0^3 are the geodetic moments for the above three models, respectively.

$$P_i^j = \beta_j \frac{1/\sigma_i^2}{\sum_{k=1}^{N_j} 1/\sigma_k^2} = \beta_j \frac{n_i}{\sum_{k=1}^{N_j} n_k} \quad (2)$$

$$\sum_{j=1}^{N_f} \sum_{i=1}^{N_j} P_i^j = 1 \quad (3)$$

where P_i^j is the weight for the i th data point in the j th data set, N_j the number of the data points in the j th data set, σ^2 the variance of the data points, n the quadrant size from quadtree sampling, β_j the weight ratio for the j th data set, and N_f is the number of data sets. In this study, we set a ratio of 50% to IP2 for its higher coherence, and 25% to IP1 and IP3, respectively.

3.2. Uniform slip model

We invert the source parameters using an elastic dislocation model in a homogeneous isotropic half-space (Okada, 1985). We first model the fault using a seven-segment uniform slip model (Model 1). For each segment, the coordinates x_0 , y_0 , length and strike are fixed, and the absolute value of rake is constrained smaller than 90° , which allows only left-lateral slip for the strike-slip component. We assume the top edges intersect the surface. The orbit error for each data set is fitted by a bilinear ramp. Particularly, we estimate the constant offset for each side of IP2 separately, as it was completely split into two halves by the fault. Therefore, there are 28 fault source parameters and 10 bilinear ramp parameters in the uniform slip model.

The surface displacements are nonlinear functions. We use a genetic algorithm (GA) to determine the optimal model which minimizes the weighted misfits between the observations and the synthetic values (Carroll, 1996). The best-fit source parameters are listed in Table 3, and the synthetic interferograms and residuals are shown in Fig. 6. The maximum slip is 5.5 m with a depth of 11 km on the fourth segment. The slip is smaller than 7.0 m in Peltzer et al. (1999), who used a single-segment uniform slip model and fixed the width as 8 km. The slip rate is also smaller than that in Funning (2005), in which the fault width is also smaller than ours. The average dip of the uniform slip model is about 93° northward and the average rake is about -2° , which suggests a nearly vertical pure left-lateral strike-slip fault. The estimated geodetic moment is 1.77×10^{20} Nm ($M_w 7.47$), similar to the seismological results. The RMS between the observations and the synthetic displacements is 41 mm.

3.3. Distributed slip model

Although the uniform slip model can provide a fair fit to the observations, it is not physically reasonable due to the sharply discontinuous slip between adjacent segments. To obtain more realistic solutions, we use the following distributed slip model.

In the distributed slip model, the width of the fault is extended to 20 km, and the length is increased by 5 km for segments 1 and 7 in order to account for the whole fault plane in the model. The fault plane is then discretized into 225 patches, each of them $4 \text{ km} \times 4 \text{ km}$. We fix the geometric parameters from the uniform slip solutions and solve for the optimal slip on each patch. The surface displacements are then the linear functions of dislocations. To determine such

Table 3
Best-fit fault parameters in the uniform slip model

No.	Slip (m)	x_0 (km)	y_0 (km)	Length (km)	Width (km)	Strike ($^\circ$)	Dip ($^\circ$)	Rake ($^\circ$)
1	1.4	-17.0	-69.5	32.5	7.5	263.3	85.5	0.8
2	2.3	-7.1	-44.0	27.8	9.2	246.5	81.6	0.7
3	2.8	-4.8	-19.7	24.3	12.6	267.4	104.7	-3.2
4	5.5	0.0	0.0	20.3	10.9	256.3	101.1	0.4
5	5.0	3.1	23.3	23.5	10.1	262.4	91.1	-1.6
6	3.9	8.4	46.3	23.6	9.0	257.0	103.0	0.5
7	4.7	17.8	61.4	17.8	4.2	238.1	80.9	-8.2

Coordinates x_0 , y_0 correspond to the top-right corner of each segment. The top edges are assumed to intersect the surface. Origin is taken to be at (35.252N, 87.307E).

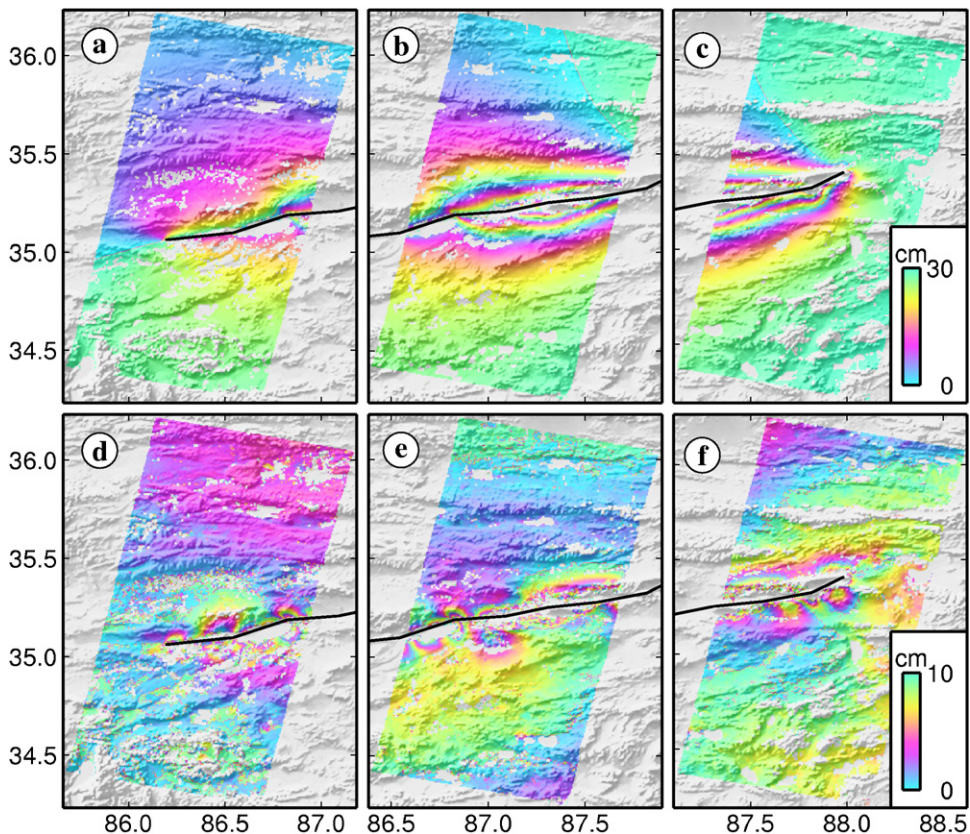


Fig. 6. (a–c) Synthetic interferograms and (d–f) residuals for the seven-segment uniform slip model.

a slip model, we set up the following equations:

$$\begin{bmatrix} \mathbf{d} \\ 0 \end{bmatrix} = \begin{bmatrix} \mathbf{G} & \mathbf{H} \\ \kappa^2 \nabla^2 & 0 \end{bmatrix} \begin{bmatrix} \mathbf{m} \\ \mathbf{t} \end{bmatrix} \quad (4)$$

where \mathbf{d} is a vector containing the observed displacements, \mathbf{G} a matrix containing Green's functions (e.g., Okada, 1985), ∇^2 is a second-order finite difference approximation of the Laplacian operator and the Lagrange multiplier κ^2 determines the weight of smoothing (Harris and Segall, 1987), \mathbf{H} a matrix containing the coordinates of the data points, and \mathbf{t} is a vector containing the bilinear ramp coefficients to correct the orbit errors.

We solve the system of Eq. (4) using a bounded variable least-squares (BVLS) method (Stark and Parker, 1995), which can seek the bounded variables to minimize the following objective function,

$$\Phi = \|\mathbf{W}(\mathbf{d} - \mathbf{G}\mathbf{m} - \mathbf{H}\mathbf{t})\|_{L2} + \|\kappa^2 \nabla^2 \mathbf{m}\|_{L2} \quad (5)$$

where \mathbf{W} is the matrix from Cholesky decomposition of weight matrix \mathbf{P} , i.e., $\mathbf{W}^T \mathbf{W} = \mathbf{P}$.

We first allow only pure left-lateral strike-slip (Model 2). The best-fit slip distribution depends on the smoothing factor κ^2 , so we show the tradeoff between weighted misfit and solution roughness in Figs. 7 and 8 (Jónsson et al., 2002). We pick the model with $\kappa = 0.10$ as a result because of its good compatibility between weighted misfit and solution roughness.

In the model, the maximum strike-slip is 5.8 m on the boundary between the 4th and 5th segment. The final RMS is 36 mm with solution roughness of 18 mm/km, which is smaller than the RMS of the uniform slip model. The synthetic interferograms and residuals in Fig. 9 show that the residuals on the boundary of adjacent segments are much smaller than that of the uniform model. We find a geodetic moment of 1.99×10^{20} Nm ($M_w 7.50$), which does not change too much for different smoothing factors.

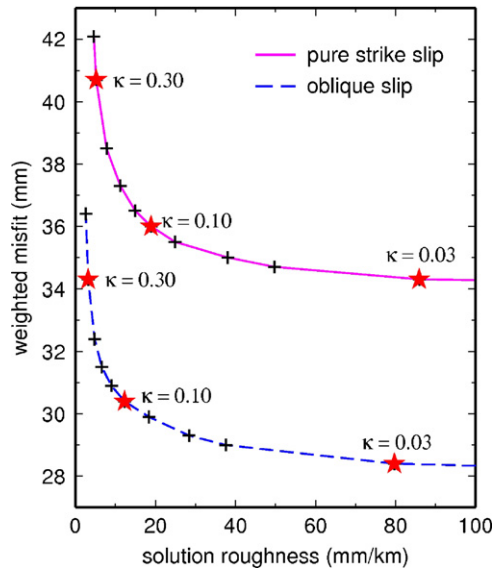


Fig. 7. Tradeoff between weighted misfit and solution roughness for the pure strike-slip model (solid line) and the oblique slip model (dashed line). Stars indicate the smoothing factors ($\kappa = 0.03, 0.10, 0.30$) used in the inversions shown in Fig. 8.

Although the pure strike-slip model can already fit the observations quite well, most seismological results show a little dip-slip for the Manya earthquake (e.g., Velasco et al., 2000). Therefore, we further estimate the slip distribution using an oblique slip model (Model 3). In this model, the strike-slip components are still constrained as left-lateral, but no constraints are utilized for the dip-slip components. From Fig. 7, we choose the solution with smoothing factor $\kappa = 0.10$ and show the slip distribution in Fig. 10. We find a maximum strike-slip of 5.6 m and a maximum dip-slip of -1.5 m. The final RMS is 30 mm with solution roughness of 13 mm/km, smaller than the RMS of the pure strike-slip model. We find a geodetic moment of 1.91×10^{20} Nm ($M_w 7.49$). The synthetic interferograms and residuals are shown in Fig. 11.

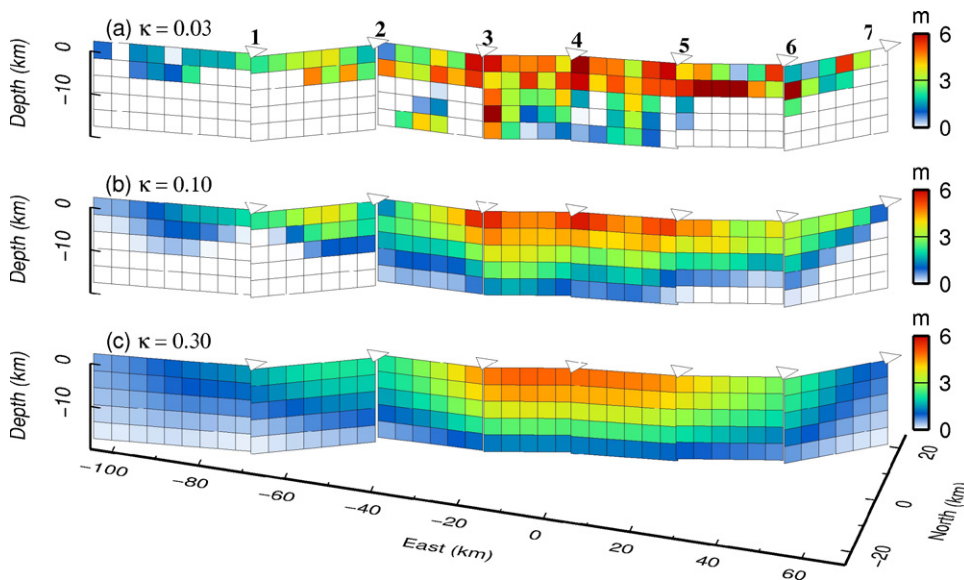


Fig. 8. Pure strike-slip models using different smoothing factors: (a) $\kappa = 0.03$, (b) $\kappa = 0.10$, and (c) $\kappa = 0.30$. We pick the second model as a result because of its good compatibility between weighted misfit and solution roughness. The numbers above the triangles indicate the segments.

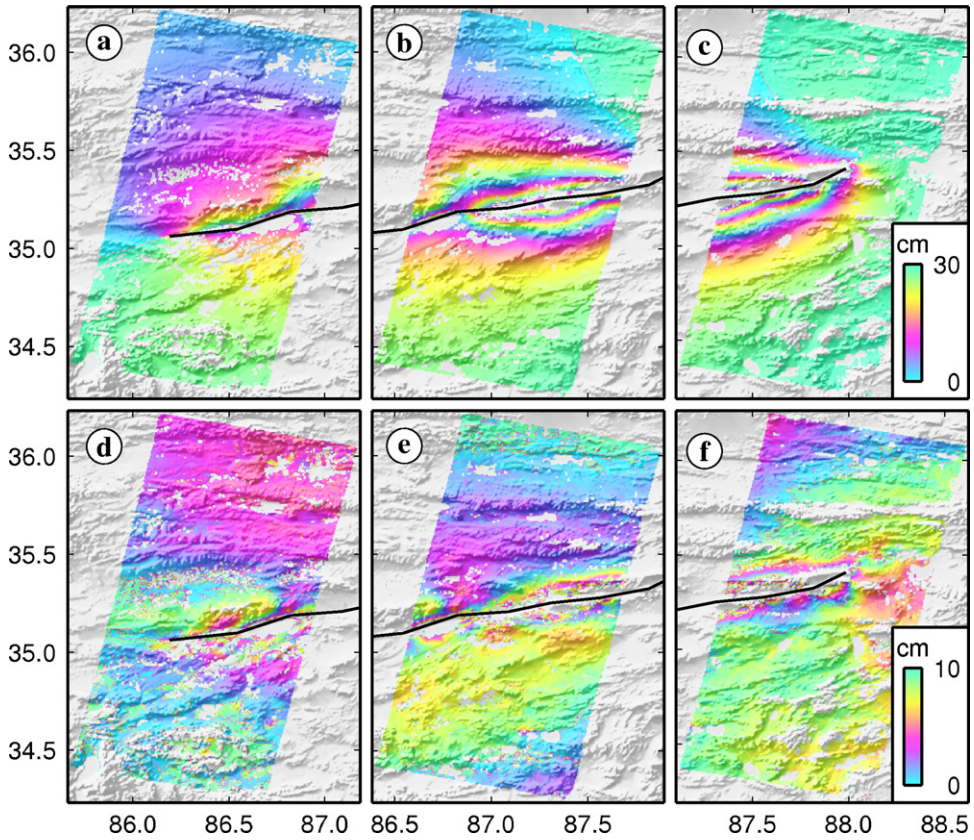


Fig. 9. (a–c) Synthetic interferograms and (d–f) residuals for the pure strike-slip model.

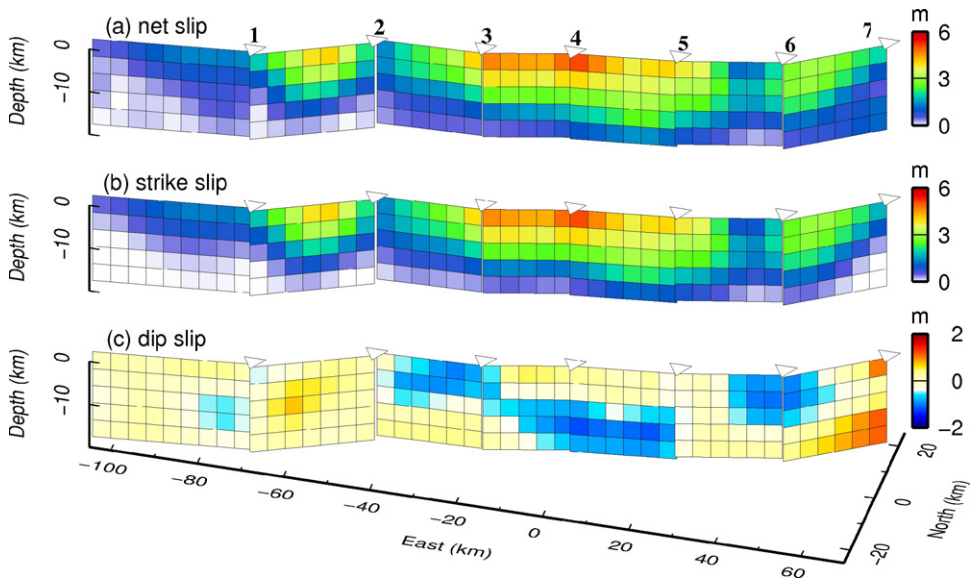


Fig. 10. Oblique slip model using smoothing factor $\kappa = 0.10$. (a) Net slip; (b) strike-slip components; (c) dip-slip components.

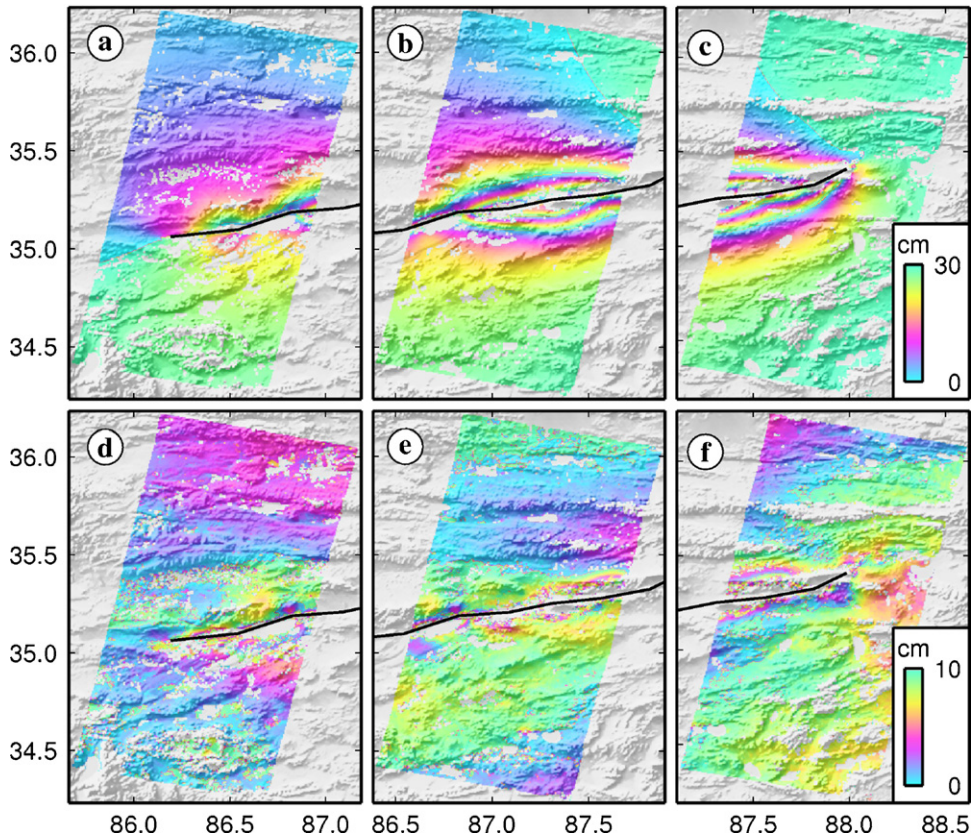


Fig. 11. (a–c) Synthetic interferograms and (d–f) residuals for the oblique slip model.

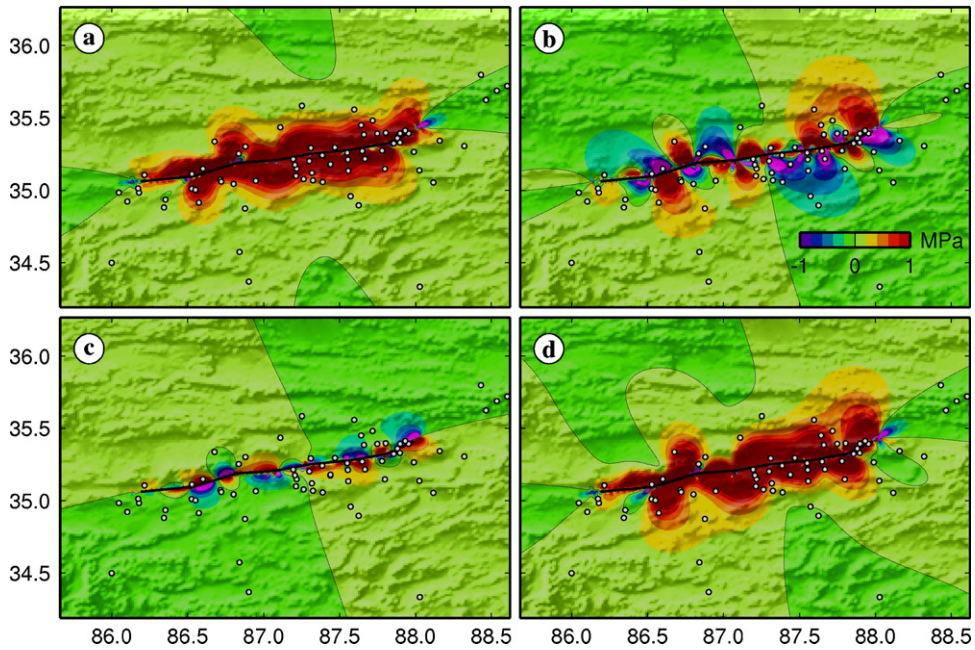


Fig. 12. Coulomb stress changes associated with the Manji earthquake. (a) Shear stress changes; (b) normal stress changes; (c) pore pressure changes; (d) Coulomb stress changes. The friction coefficient of 0.75 and the Skempton coefficient of 0.5 are used for the Coulomb stress computation (Árnadóttir et al., 2003).

We use the fault solution from the oblique slip model to compute the Coulomb stress change (ΔCFS) around the fault, at depth of 5 km.

$$\Delta\text{CFS} = \Delta\tau_s + \mu(\Delta\sigma_n + \Delta p) \quad (6)$$

where $\Delta\tau_s$ is the change in shear stress, $\Delta\sigma_n$ the change in normal stress (positive for extension), Δp the change in pore pressure, and μ is the coefficient of friction, ranging from 0.6 to 0.8 for most rocks (Harris, 1998; Árnadóttir et al., 2003).

Fig. 12 shows the changes in shear stress, normal stress, pore pressure, and Coulomb stress. Almost all aftershocks occurred in the areas with Coulomb stress increase (Fig. 12d). The large stress drop in Fig. 12 suggests that most energy was released during the mainshock near the fault, that is why few moderate aftershocks occurred for the large Manyi earthquake.

4. Discussion and conclusions

We investigate the coseismic deformation and slip distribution of the 1997 M_w 7.5 Manyi earthquake using InSAR measurements. The fault trace is constrained by the combination of interferometric coherence image and azimuth offset image. We propose the TXOR algorithm to remove the temporal decorrelation in the interferometric coherence image. We estimate the source parameters using both uniform and distributed slip models in an elastic half-space, and find that the distributed oblique slip model gives the best solution to fit the observations. In the best-fit model, we find a maximum strike-slip of 5.6 m and a maximum dip-slip of -1.5 m. The estimated geodetic moment is 1.91×10^{20} Nm (M_w 7.49), of which almost 68% released in the uppermost 8 km, and 82% in the uppermost 12 km of the brittle crust.

InSAR has been proven a powerful technique to measure coseismic deformation with centimeter precision in California (e.g., Jónsson et al., 2002), Alaska (e.g., Wright et al., 2004), Turkey (e.g., Bürgmann et al., 2002), Iceland (e.g., Pedersen et al., 2003) and other regions for which both remote and ground-motion data are available. The distributed slip models are also routinely used to analyze the coseismic deformation measured by geodetic techniques. The InSAR-based slip distributions are often in good agreement with those obtained from GPS observations (e.g., Bürgmann et al., 2002; Wright et al., 2004). In this study, all the coseismic pairs have high coherence (Fig. 3) and short perpendicular baselines (less than 100 m in Table 1), which are the most important factors for the high-quality InSAR observations. Therefore, we suggest the coseismic displacements and slip distribution are reliable even though no ground-motion data are available to validate the results.

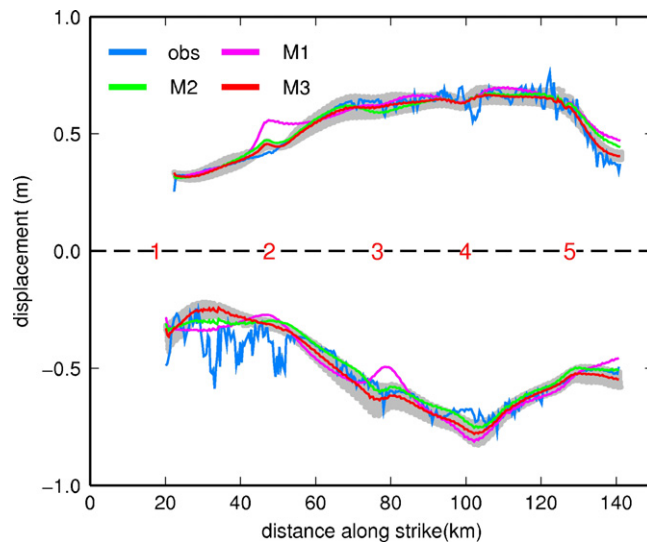


Fig. 13. Observed and synthetic displacement profiles. obs: observed displacements; M1: synthetic displacements using Model 1; M2: synthetic displacements using Model 2; M3: synthetic displacements using Model 3. Gray dots denote all synthetic displacements in the 10 km bins using Model 3. The central broken line indicates the fault location and the segment numbers.

An important feature of the Manyi earthquake is the asymmetric displacements on the opposite sides of the fault. Possible explanations for the asymmetry include across-fault contrasts in the effective shear modulus of the host rocks, postseismic relaxation in the presence of lateral variations in the effective viscosity of the substrate, multiple sub-parallel shear zones, and a non-vertical fault geometry (Fialko, 2006). Multiple sub-parallel shear zones are unlikely explanations for the Manyi earthquake, because even the nearest Altyn Tagh fault is too far from the Manyi fault to affect the coseismic deformation. We suggest that the contribution to the asymmetric deformation by the postseismic transients can also be neglected, because IP2 only covers one-week postseismic deformation. Peltzer et al. (1999) found the asymmetry could not be well modeled using linear elastic model with a straight vertical fault. They suggested the elastic moduli of the crust in tension and compression are different, and a ratio of 2 between compressive and tensile elastic moduli could account for the observed asymmetry. Funning (2005) found a reversal of dip between the eastern (No. 1–4 in Funning, 2005) and the western (No. 5–9) segments of the hypocenter. In his model, all of the western segments dip southward ($>90^\circ$) and all of the eastern segments dip northward (82°). Fig. 13 shows the profiles of the observed and the synthetic displacements about 5 km away from the fault trace in this study. We find that all models in this study can fit the asymmetric pattern quite well, and the distributed oblique slip model is the best of all. However, we do use the linear elastic model and the dips of the segments 3–7 are all larger than 90° , i.e., there is no distinct reversal between the opposite sides of the hypocenter. Therefore, from the models in this study, we suggest that the non-vertical fault geometry and the variation of dips between adjacent segments are another reasonable explanation for the asymmetry.

Acknowledgements

We thank the Editor Prof. Giorgio Ranalli, Dr. Gail Atkinson and an anonymous reviewer for their detailed and constructive reviews of the manuscript. We thank Prof. Philip B. Stark and Prof. Robert L. Parker for suggestions on BVLS program, and Dr. Gareth J. Funning and Dr. Tim J. Wright for discussions on phase unwrapping. ERS data were provided by the European Space Agency under a category 1 proposal (ID 3392). The GMT software was used to prepare all the figures (Wessel and Smith, 1998). This work was supported by Research Fund for the Program for New Century Excellent Talents in University (NCET-04-0681), NSFC (No. 40574006), a Specialized Research Fund for the Doctoral Program of Higher Education (No. 20030486038), and the foundation of LOGEG State Bureau of Surveying and Mapping (No. 04-01-08).

References

- Árnadóttir, T., Jónsson, S., Pedersen, R., et al., 2003. Coulomb stress changes in the South Iceland Seismic Zone due to two large earthquakes in June 2000. *Geophys. Res. Lett.* 30 (5), 1205, doi:10.1029/2002GL016495.
- Bürgmann, R., Ayhan, M.E., Fielding, E.J., et al., 2002. Deformation during the 12 November 1999 Düzce, Turkey, earthquake, from GPS and InSAR data. *B. Seismol. Soc. Am.* 92 (1), 161–171.
- Carroll, D.L., 1996. Genetic algorithms and optimizing chemical Oxygen-Iodine Lasers. In: Wilson, H.B., Batra, R.C., Bert, C.W., et al. (Eds.), *Developments in Theoretical and Applied Mechanics, XVIII*. School of Engineering, The University of Alabama, pp. 411–424.
- Chen, C.W., 2001. Statistical-cost network-flow approaches to two-dimensional phase unwrapping for radar interferometry. Ph.D. Thesis, Stanford University.
- Farr, M., Kobrick, M., 2000. Shuttle Radar Topography Mission produces a wealth of data. *EOS Trans.* 81, 583–585.
- Fialko, Y., 2006. Interseismic strain accumulation and the earthquake potential on the southern San Andreas fault system. *Nature* 441, 968–971.
- Funning, G.J., 2005. Source parameters of large shallow earthquakes in the Alpine-Himalayan belt from InSAR and waveform modelling. Ph.D. Thesis, University of Oxford.
- Harris, R.A., 1998. Introduction to special section: Stress triggers, stress shadows, and implications for seismic hazard. *J. Geophys. Res.* 103 (B10), 24,347–24,358.
- Harris, R.A., Segall, P., 1987. Detection of a locked zone at depth on the Parkfield, California, segment of the San Andreas fault. *J. Geophys. Res.* 92 (B8), 7945–7962.
- Jónsson, S., Zebker, H., Segall, P., et al., 2002. Fault slip distribution of the 1999 M_w 7.1 Hector Mine, California, earthquake, estimated from satellite radar and GPS measurements. *B. Seismol. Soc. Am.* 92 (4), 1377–1389.
- Lasserre, C., Peltzer, G., Crampé, F., et al., 2005. Coseismic deformation of the 2001 M_w = 7.8 Kokoxili earthquake in Tibet, measured by synthetic aperture radar interferometry. *J. Geophys. Res.* 10, B12408, doi:10.1029/2004JB003500.
- Massonnet, D., Rossi, M., Carmona, C., et al., 1993. The displacement field of the Landers earthquake mapped by radar interferometry. *Nature* 364, 138–142.
- Masterlark, T., Lu, Z., 2004. Transient volcano deformation sources imaged with interferometric synthetic aperture radar: application to Seguam Island, Alaska. *J. Geophys. Res.* 109, B01401, doi:10.1029/2003JB002558.

- Okada, Y., 1985. Surface deformation due to shear and tensile faults in a half-space. *B. Seismol. Soc. Am.* 75 (4), 1135–1154.
- Pedersen, R., Jónsson, S., Árnadóttir, T., et al., 2003. Fault slip distribution of two June 2000 M_w 6.5 earthquakes in South Iceland estimated from joint inversion of InSAR and GPS measurements. *Earth Planet Sci. Lett.* 213, 487–502.
- Peltzer, G., Crampé, F., King, G., 1999. Evidence of the nonlinear elasticity of the crust from M_w 7.6 Manyi (Tibet) earthquake. *Science* 286, 272–276.
- Scharroo, R., Visser, P., 1998. Precise orbit determination and gravity field improvement for the ERS satellite. *J. Geophys. Res.* 103 (C4), 8113–8127.
- Simons, M., Fialko, Y., Rivera, L., 2002. Coseismic deformation from the 1999 M_w 7.1 Hector Mine, California, earthquake as inferred from InSAR and GPS observations. *B. Seismol. Soc. Am.* 92 (4), 1390–1402.
- Stark, P.B., Parker, R.L., 1995. Bounded variable least squares: an algorithm and applications. *Computat. Stat.* 10, 129–141.
- Tapponnier, P., Molnar, P., 1977. Active faulting and tectonics in China. *J. Geophys. Res.* 82, 2905–2930.
- Van der Woerd, J., Ryerson, F.J., Tapponnier, P., et al., 2000. Uniform slip-rate along the Kunlun fault: Implications for seismic behavior and large-scale tectonics. *Geophys. Res. Lett.* 27 (6), 2353–2356.
- Velasco, A.A., Ammon, C.J., Beck, S.L., 2000. Broadband source modeling of the November 8, 1997, Tibet ($M_w = 7.5$) earthquake and its tectonic implications. *J. Geophys. Res.* 105 (B12), 28,065–28,080.
- Wang, H., Ge, L., Xu, C., et al., 2007. 3-D coseismic displacement field of the 2005 Kashmir earthquake inferred from satellite radar imagery. *Earth Planets Space* 59 (5), 343–349.
- Wang, Q., Zhang, P.-Z., Freymueller, J.T., et al., 2001. Present-day crustal deformation in China constrained by Global Positioning System measurements. *Science* 294, 574–577.
- Wessel, P., Smith, W.H.F., 1998. New, improved version of generic mapping tools released. *EOS Trans.* 79 (47), 579.
- Wright, T.J., Lu, Z., Wicks, C., 2004. Constraining the slip distribution and fault geometry of the M_w 7.9 3 November 2002 Denali Fault earthquake with interferometric synthetic aperture radar and global positioning system data. *B. Seismol. Soc. Am.* 94 (6B), S175–S189.
- Zhang, P.-Z., Shen, Z., Wang, M., et al., 2004. Continuous deformation of the Tibet Plateau from global positioning system data. *Geology* 32 (9), 809–812.